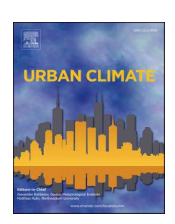


Contents lists available at ScienceDirect

Urban Climate

journal homepage: www.elsevier.com/locate/uclim





Impact of growth of a medium-sized Indian coastal city on urban climate: A case study using data fusion and analytics

Udaysankar S. Nair^{a,*}, Christopher Phillips^a, Sukanya Dasgupta^b, Chandana Mitra^b

- ^a Atmospheric and Earth Science Department, University of Alabama in Huntsville, Huntsville, AL, USA
- ^b Geosciences Department, Auburn University, Auburn, AL, USA

ARTICLE INFO

Keywords: Land use land cover (LULC) Microclimate Small and medium sized cities (SMSC) Trivandrum city Google earth engine (GEE) Moderate resolution imaging Spectroradiometer (MODIS)

ABSTRACT

In India, unlike mega cities, little is known about how the growth of small and medium-sized cities (SMSC) impacts urban climate. Further, such impacts are amplified in coastal settings. We use data fusion and analytics to study how the growth of Thiruvananthapuram, a typical medium-sized coastal city in India, modifies the urban climate. The datasets used are National Aeronautics and Space Administration (NASA) Moderate Resolution Imaging Spectroradiometer (MODIS) land products, NASA Modern-Era Retrospective analysis for Research and Applications (MERRA-2) and Indian Meteorological Department surface observations contained within the National Oceanic and Atmospheric Administration (NOAA) global compilation of in-situ observations. The study found a \sim 48% increase in urban and built-up land cover over the last two decades, causing an increase in albedo, surface roughness and a decrease in emissivity and moisture availability. Decreasing moisture availability most affected air temperature, with urban growth adding to large-scale climatic trends of increasing monthly mean daily maximum (+1 °C), minimum (+0.4 °C) and average temperatures (+0.22 °C). Sea-breeze circulation strengthened in response to increasing coastal urbanization and the inland propagation modified with increased convergence and (potentially) rainfall, near the coast.

1. Introduction

While all cities have the potential to impact urban climate and exacerbate natural hazards (Rosenzweig et al., 2018), the majority of the existing studies on this topic are dedicated to megacities (Lamb et al., 2019; Yang et al., 2019). This is also true for India's urban system, which is top-heavy with a few big cities containing the maximum population but also has several small and medium-sized cities (SMSC) experiencing rapid growth (Shaban et al., 2020). Prior studies on urban impacts on climate, climate adaptation, and mitigation techniques are all focused on Indian mega cities (Shaban et al., 2020; Rana and Krishan, 1981; Mohan and Kandya, 2015). Thus, there is a significant knowledge gap regarding the urban climate variability of SMSCs and the feasible adaptation and mitigation strategies for future scenarios. Taking into consideration the fast-paced growth of SMSCs, there is an urgent need to address this knowledge gap and recommend mitigation strategies (Birkmann et al., 2016), so that Indian SMSCs become more prepared and resilient to extreme weather events including heat waves, floods, and thunderstorms.

While urbanization occurs in all geographical settings, it has been hypothesized that its impacts on clouds and rain are amplified in

^{*} Corresponding author.

E-mail addresses: nairu@uah.edu (U.S. Nair), cep0013@uah.edu (C. Phillips), szd0086@auburn.edu (S. Dasgupta), czm0033@auburn.edu (C. Mitra).

coastal settings (Mahmood and Coauthors, 2014). This is because the dynamic and thermodynamic perturbations caused by urbanization can consistently interact with sea and land breeze circulation and cause changes in clouds and rainfall. Even though such amplification has been identified as an important research priority (Mahmood and Coauthors, 2014), studies are still lacking, especially for SMSCs.

The primary goal of this study is to utilize the fusion of satellite, *in situ* observations, and atmospheric reanalysis datasets to examine the growth of a typical Indian coastal SMSC and to gain an understanding of how it affects land-atmosphere interactions and urban climate.

This manuscript is organized as follows. The study area is described in section 2. The data sets and analysis methodology utilized are described in section 3 and 4, respectively. Detailed results of the analysis are presented in section 5. Broader context and summary findings for this study are presented in sections 6 and 7 respectively.

2. Study area

SMSCs are prevalent along the coastal regions of India, and Thiruvananthapuram Municipal Corporation (TMC) is a typical example (Fig. 1a) which will be the focus of this study. TMC is located on the southwestern coast of India, with the western border bounded by the Arabian Sea and the mountainous terrain of the Western Ghats located ~30 km northeast of the eastern border. In addition to year-round influences of sea breeze circulations, Thiruvananthapuram is affected by large-scale monsoonal circulation at seasonal timescales (Anurose et al., 2018). Meteorological observations from the city are crucial to assessing the onset of the monsoon. During the monsoon season, offshore airflow, potentially modified by urban interactions, becomes the source for orographic clouds that produce heavy rainfall in the upwind regions of the Western Ghats. In recent years, monsoon rainfall has intensified, causing flooding and landslides (Hunt and Menon, 2020).

Population changes within TMC and in its surroundings show that it is one of the SMSCs experiencing fast-paced growth (Fig. 1b). TMC covers an area of $214 \, \mathrm{km}^2$, and the population estimate given by the $2011 \, \mathrm{census}$ is 957,730. The population growth curve for the urban agglomeration of the TMC and surroundings (United Nations, 2018) shows a sharp increase around the year 2000, with the growth rate further steepening around 2010. Since the most recent census (2011) shows that $\sim 60\%$ of the population within the agglomeration resides within TMC, this growth pattern is also applicable to TMC. The current trend of steep growth rate is projected to hold in the coming decades.

To the best of our knowledge, prior research has not adequately quantified the LULC change of TMC caused by the fast-paced population growth during the last two decades nor the associated impact of increased urban built-up land cover.

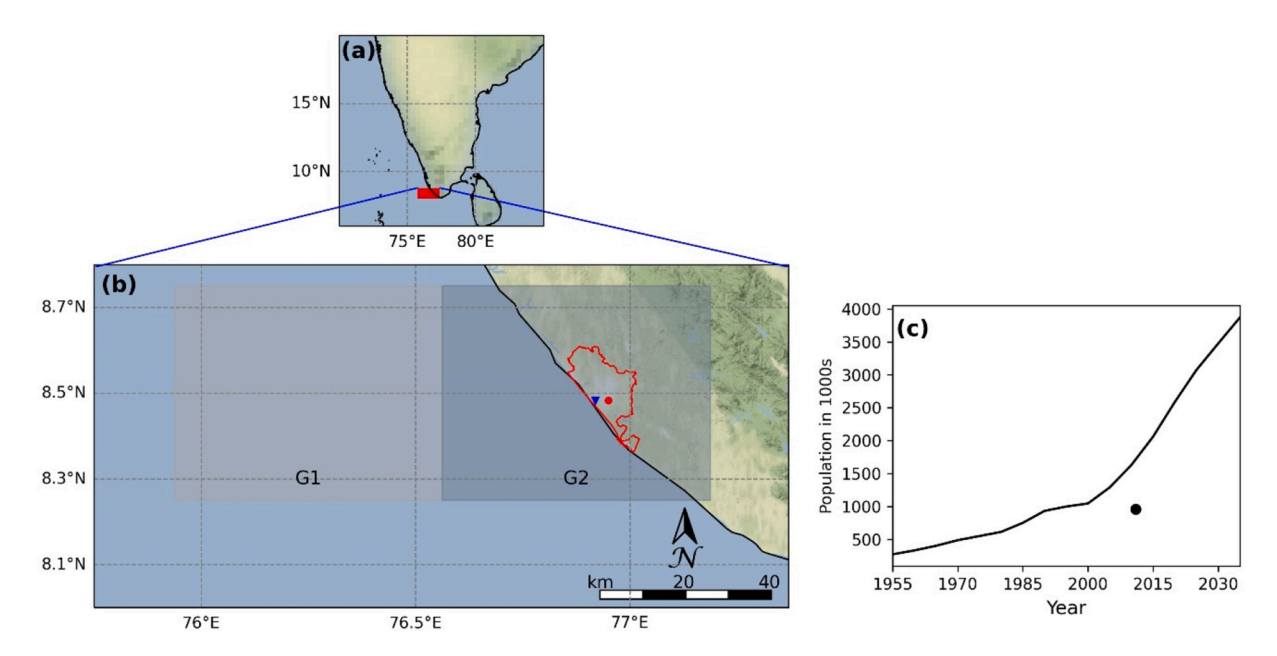


Fig. 1. a) The red rectangular box shows the location of the study area along the southwestern coast of the Indian subcontinent, with the enlarged view shown in panel b; b) The boundaries of the Thiruvananthapuram Municipal Corporation, the administrative region that constitutes the city of Thiruvananthapuram, are shown using the red outline. Ocean and land areas are shown using blue coloring and shaded terrain relief, respectively. The triangular and circular markers show the locations of coastal and inland meteorological stations (discussed in section 2), respectively. The light and dark gray shaded regions show the footprints of the two reanalysis grid cells (discussed in section 2), respectively (G1 and G2); c) Census estimates and projected population growth (thousands) for the Thiruvananthapuram urban agglomeration (United Nations, 2018) from 1955 to 2035. The disc-shaped marker shows the population estimate for Thiruvananthapuram city from the 2011 census. (For interpretation of the references to colour in this figure legend, the reader is referred to the web version of this article.)

3. Data used

We utilize three sources of data for fusion and analysis of urban impacts on climate (see the first column in Fig. 2) including satellite, *in situ* meteorological observations and gridded reanalysis data. Details of these datasets are provided in the following sections.

3.1. Satellite observations

We characterize and quantify alternations in LULC change and associated land surface properties within TMC using a variety of land surface products derived from the Moderate Resolution Spectroradiometer (MODIS) sensor onboard NASA's Terra satellite. The Terra satellite is in a sun-synchronous orbit and crosses the equator at 1030 L16 a 16-day repeat cycle (Wolfe et al., 1998). Note that monitoring of the earth and atmosphere by sensors on the NASA Earth Observing System (EOS) Terra platform started in 1999, coinciding with the sharp increase in population growth over TMC (Fig. 1b) and allowing for quantifying LULC changes and land surface characteristics within the TMC during the multi-decadal period of 2000–2019. Specifically, we use the following MODIS-derived land products:

- 1. MODIS global land cover classification (LCC) product is used to analyze changes in LULC, available annually at 500 m spatial resolution (Channan et al., 2014) and described using the seventeen International Geosphere-Biosphere Programme (IGBP) land cover classifications of which eleven are natural vegetation, three are human-impacted, and three are non-vegetated. LCC categories relevant to the study area include evergreen needleleaf forest (EN), woody savannas (WS), savannas (SV), grasslands (GL), permanent wetlands (WL), croplands (CL), urban and built-up lands (UB), cropland/natural mosaics (CN) and water bodies (WB).
- 2. LULC change results in the alteration of land surface properties including LST, vegetation cover, albedo, and emissivity. We employed the 1 km resolution, 8-day composite of land surface temperature (LST) and emissivity product (MOD11A2) to study modifications in LST and emissivity associated with LULC change. The MOD11A2 product is based on the split-window algorithm (Wan et al., 2002) and relies on 10.78–11.28 μm and 11.77–12.27 μm infrared channels to retrieve LST and emissivity. Mean retrieval errors for LST are within 2.0 K and have a standard deviation of ~0.5 K (Wan, 2014). Daytime and nighttime LST retrievals are available as a part of the MOD11A2 product, and both are used in this study. We applied the global MODIS normalized difference vegetation index (NDVI) product to characterize changes in green vegetation cover. The MODIS NDVI used in this study is a sixteen-day composite, available at 250 m resolution. The value of NDVI, which is the normalized difference between red and near-infrared reflectance, ranges between 1 and 0 and is indicative of the fractional cover of green vegetation of a pixel (Didan et al., 2015). To investigate modifications in land surface albedo caused by LULC change, we studied the 500 m spatial resolution MODIS sixteen-day composite broadband white-sky albedo product (MCD43A3). Note that white-sky albedo is the albedo considering only the diffuse component of the solar radiation as opposed to black-sky albedo which is based only on the direct component. We use

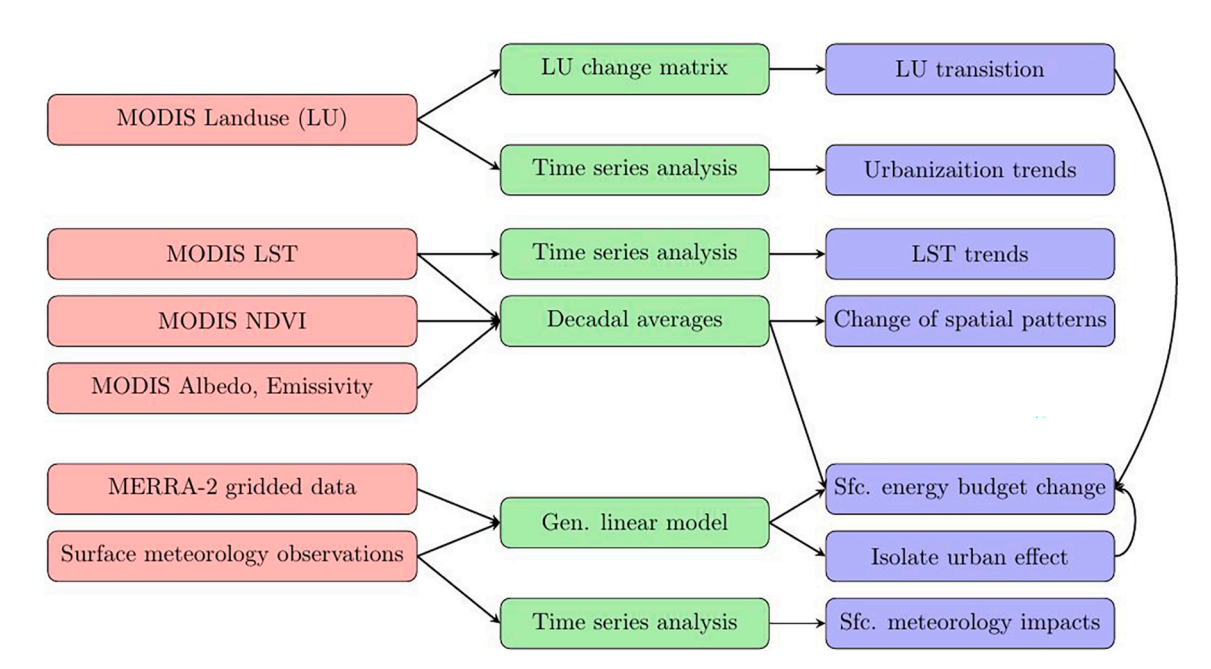


Fig. 2. Overview of the data fusion and analytic methodology. Light red, green and blue blocks in the flow chart denote datasets, analytic methodology and outcomes, respectively. (For interpretation of the references to colour in this figure legend, the reader is referred to the web version of this article.)

white-sky albedo in our analysis since it is closest to broadband albedo values used for surface energy budget computations (Wang et al., 2004).

Note that the above-described data is cloud accessible through Google Earth Engine (GEE). GEE is a planetary-scale cloud-computing platform that provides not only seamless access to >40 years of satellite imagery and derived products, but also a variety of algorithms to process the data. We utilize the spatial filtering capability of GEE to filter the MODIS data using a shapefile of the TMC.

3.2. Surface meteorological observations

We utilize monthly average summaries and hourly observations derived from a global compilation of *in-situ* surface meteorological observations (including those from Indian Meteorological Department (IMD) stations) maintained by the National Oceanic and Atmospheric Administration (NOAA) for statistical modeling. Monthly climate summaries from this compilation are the Global Historical Climatology Network monthly (referred from here on as GHCNm) summaries version 3 (Lawrimore et al., 2011) dataset and is cloud accessible through the National Center for Environmental Information (NCEI). We utilize the GHCNm data for statistical modeling.

We also use the hourly observations derived from the compilation available as the Integrated Surface Database (ISD) hourly records (Smith et al., 2011) and cloud accessible through the National Center for Environmental Information (NCEI). We utilized ISD data for examining the geographic variability of urban impact on surface meteorology.

We used both monthly summaries and hourly observations for two specific surface stations, namely Thiruvananthapuram City (IMD station, WMO # 43371) and Thiruvananthapuram Airport (IMD station, WMO # 43372). Thiruvananthapuram station is located near the center of the urban core (referred from hereon as the inland station), while Thiruvananthapuram Airport station is situated at the periphery of the urban core and near the coast (referred from hereon the coastal station). The inland and coastal stations are shown using circular and triangular markers in Fig. 1b.

3.3. Reanalysis data

The NASA Modern-Era Retrospective analysis for Research and Applications 2 (MERRA-2) dataset is a coherent, gridded best estimate of atmospheric conditions derived using a consistent modeling system subject to observational constraints. MERRA-2 is available on a global grid with a spacing of 0.5° x 0.625° and the period of 1980-present and is produced using the Goddard Earth Observing System (GEOS) atmospheric model assimilating space-based remote sensing and *in-situ* observations using 3D variational data assimilation. Additionally, MERRA-2 also incorporates aerosol distributions from the Goddard Chemistry, Aerosol, Radiation, and Transport (GOCART) model (Gelaro and Coauthors, 2017). The MERRA-2 dataset includes upper atmospheric variables at three-hourly intervals and surface atmospheric, ocean and land surface variables at hourly intervals.

We utilize MERRA-2 variables from two grid point locations, one approximately centered over TMC (8.5 N, 76.875E, referred from here on as G2, Fig. 1a) and the second grid point located to the west of G2 (8.5 N, 76.25E, referred from here on as G1, Fig. 1a). In combination with surface observations, MERRA-2 variables from these grid points are utilized for statistical modeling.

4. Methodology

An overview of the major components of our data fusion and analytic methodology is shown in Fig. 2 and the details of which are provided in the following sections. When appropriate, a few minor aspects of the approach are described in the results section.

4.1. Satellite data analysis of LULC change and land surface properties

To examine spatial patterns of multi-decadal changes in LULC, spatial maps of the same are constructed for the years 2001 (the first year of the 2000–2009 decade for which LULC data is available) and 2019 (the last year of the 2010–2019 decade) using MODIS LCC dataset. We also constructed a LULC change matrix that quantifies areal changes of all possible LULC transitions between the years 2001 and 2019. Additionally, the area of urban and built-up land cover within TMC is computed on an annual basis from 2001 through 2019. A linear model was fit to the resulting time series for the 2001-2009 and 2010-2019 time periods and was used to quantify growth rates of areal extent of urban and built-up land cover. The annual changes in urban land cover were calculated as the percentage annual growth rate (AGR) (Xiao et al., 2006) for a given year t defined as:

$$AGR(t) = \frac{UB(t) - UB(t-1)}{\tau_{AU}} \times 100\%$$
(1)

where UB(t) and UB(t-1) are the areas of the urban and built-up land cover for years t and t-1 within an administrative unit (TMC in this case) with a total area of τ_{AU} .

We examined the impact of urbanization on the spatial variability of land surface characteristics discussed previously, by computing decadal averages of day and nighttime LST, NDVI, albedo and emissivity for the periods of 2000–2009 and 2010–2019. Averages are calculated for each pixel at the native product resolution, and spatial maps are made to compare changes in spatial patterns between the two decadal periods of 2000–2009 and 2010–2019. In addition, we also computed monthly and spatially averaged time series of day and nighttime LST for the TMC region from 2000 to 2019. We conducted a seasonal decomposition of both

the tseries to extract the seasonally adjusted component to highlight temporal changes. We then utilized Mann-Kendall seasonal tests to examine if monotonic, statistically significant trends are present in the day and nighttime LST time series. If a statistically significant, monotonic trend was detected, the rate of change was computed using the Sen slope estimator. Seasonal decomposition, Mann-Kendall seasonal testing and Sen slope estimation were conducted using the R software environment, with the decompose function, Mann-Kendall zyp packages being utilized respectively.

Note that, when computing the decadal average spatial maps and monthly and spatial average time series of LST, we applied the methodology of Hu and Brunsell (2013) to minimize the effects of cloud contamination.

The above-described analysis of satellite datasets along with *in-situ* meteorological observations is used to conduct order-of-magnitude reasoning for identifying dominant changes to the surface energy budget caused by urban growth (details provided in the results section).

4.2. Analysis of urbanization impacts on the surface meteorology of TMC

We used statistical modeling to examine the impact of urban and built-up land cover area growth on the surface air temperature. The statistical modeling approach consisted of developing three generalized linear models (GLMs) (Nelder et al., 1972) for predicting monthly mean maximum (GLM_{Tmx}), minimum (GLM_{Tmn}), and average surface temperature (GLM_{Tav}) at the location of the Thiruvananthapuram City station (IMD station, WMO # 43371). These three GLMs were developed for times before when drastic growth of urban and built-up land cover occurred within TMC, namely 1980–1999. A set of candidate predictors for these GLMs were chosen to account for both large-scale climate trends and local forcing factors, except for land cover change. Note that the choices of the variables are guided by prior studies (Dai et al., 1999; Nair et al., 2011; Phillips et al., 2022). These GLMs were then used to predict the monthly mean maximum, minimum and mean surface temperature for the period of 2000–2021. Differences between the GLM predicted trends and observed trends were utilized to quantify the effects of urbanization on monthly mean maximum, minimum and mean temperatures. When applicable, Mann-Kendall tests were used to detect monotonic trends.

The set of GLM candidate predictor variables was selected from the NASA MERRA-2 dataset. Candidate GLM predictors chosen to account for large-scale climate trends include monthly average two-meter maximum, minimum, and mean temperatures (T_{mx} , T_{mn} and T_{av}) and the zonal and meridional component of winds (U and V) for the MERRA-2 grid point immediately west of TMC (G_1 , Fig. 1a). Note that the offshore location G_1 is far enough from TMC to minimize the effects of urbanization but close enough to capture the large-scale climate trends affecting TMC. GLM predictors chosen to account for the effects of local forcing (except for LULC change) are root zone soil moisture (S_m), two-meter specific humidity (S_h), cloud optical depth (τ), cloud cover (C_h), precipitable water (C_h), and two-meter wind speed (C_h) at the MERRA-2 grid point located over TMC region (C_h 2, Fig. 1a). Specifics of candidate GLM predictor variables used for each of the GLM C_m 1, and GLM C_m 1, and GLM C_m 2 models are shown in Table 1.

Monthly means of observed values of maximum, minimum, and mean two-meter temperature from GHCNm summaries are used to fit the GLM_{Tmx} , GLM_{Tmn} and GLM_{Tav} models. Forward-backward stepwise modeling is used when fitting the GLM to narrow the candidate set of predictors (Table 1) and arrive at the most parsimonious and accurate model. Furthermore, variable inflation factor (VIF) analysis is examined to minimize multicollinearity, with variables with VIF > 5 being removed as predictors. The smaller set of predictors determined using the above-described process is shown in Table 1.

Additionally, we also intercompared average daytime patterns of surface meteorology between two decades of contrasting patterns of urban growth (2000–2009 and 2010–2019). ISD hourly records for two surface stations, namely the inland and coastal stations are used for this purpose (Fig. 1a).

For each decadal period (2000–2009 and 2010–2019), mean diurnal cycles of near-surface observations of temperature, dewpoint, and wind are computed for the inland and coastal stations. When constructing the decadal average daytime cycles, hourly reports for the coastal station were subsampled to match the three hourly frequencies at which the surface reports are available for the inland station. Then, the observations for both stations at three hourly intervals were averaged to produce a decadal mean daytime cycle for each station and also the corresponding standard deviation. We also utilized the monthly average of hourly wind observations for the Thiruvananthapuram station from the ISD to analyze long-term trends of the same for the urban core region.

Table 1 MERRA-2, candidate predictors used in the forward-backward stepwise modeling to formulate generalized linear models for monthly mean maximum, minimum, and average surface air temperatures for Thiruvananthapuram station (left column) are shown in the middle column. Predictors selected through forward-backward stepwise modeling and subsequently down-selected to minimize multicollinearity are shown in the right column. Variables shown in bold fonts are for location G_1 while the others are for location G_2 .

GLM	Candidate Predictors	Chosen Predictors
$\begin{array}{l} \text{GLM}_{\text{Tmx}} \\ \text{GLM}_{\text{Tmn}} \\ \text{GLM}_{\text{Tav}} \end{array}$	$\begin{split} &T_{mx},\ U,\ V,\ S_{m},\ S_{h},\ \tau,\ C,\ P_{w_{s}}W_{s}\\ &T_{mn},\ U,\ V,\ S_{m},\ S_{h},\ \tau,\ C,\ P_{w_{s}}W_{s}\\ &T_{av},\ U,\ V,\ S_{m},\ S_{h},\ \tau,\ C,\ P_{w_{s}}W_{s} \end{split}$	$\begin{split} &T_{mx},~U,~V,~S_{m},~C,W_{s}\\ &T_{mn},~U,~V,~S_{m},~S_{h},~\tau,W_{s}\\ &T_{av},~U,~V,~S_{m},~C,W_{s} \end{split}$

5. Results

5.1. Multi-decadal land cover changes over Thiruvananthapuram

Analysis of MODIS satellite-derived land cover shows substantial changes occurring over TMC during the last two decades (Table 2). The most dominant land cover change occurring between 2001 and 2019 is a 61% increase in the area of urban and built-up land cover from 46 km² to 73.88 km². A major portion of this increase resulted from the conversion of cropland and natural vegetation cover to urban and built-up areas. Based on the personal experience of the authors, IGBP cropland and natural vegetation cover classification in the context of TMC consists of lower-density residential areas interspersed within a mix of natural vegetation, coconut, banana *etc.*, and open areas with a variety of ground cover and small trees. Other notable and important changes include a decrease in evergreen broadleaf and wetland regions, which are of ecological importance.

Spatial patterns of land cover change over the 2001–2019 time period (Fig. 3) show substantial expansion of urban and built-up land cover, with the growth extending northwestward and closely approaching the western boundary of TMC by the year 2019. Another notable change is the strip of the main urban core located along the coast and other fragments of urban and built-up land cover to the north in the year 2001 (Fig. 3a) merge by 2019 to form a long and continuous coastal ribbon of urban development (Fig. 3b). This shows the gradual transformation of TMC into an urban agglomeration.

Temporal variation of urban and built-up land cover area (Fig. 4) shows a drastic increase in growth rate between 2001 and 2009 and 2010–2019 time period. Growth rates for these two time periods are estimated as the slope of the time series of yearly values of the area of urban and built-up land cover (Fig. 4a). The growth rates are 0.53 $\rm Km^2~Y^{-1}$ and 2.54 $\rm Km^2~Y^{-1}$ for the 2001–2009 and 2010–2019 time periods. The urban and built-up land cover increased at an average rate of 0.17% during 2000–09 which rose to an average rate of 0.68% during 2010–19 (Fig. 4b). The AGR for TMC continued to be higher during 2010–2018 and achieved a maximum value of \sim 1.92% in 2018.

Decadal average spatial patterns of the day, nighttime LST, and NDVI all show notable changes that correlate well with patterns of land cover change (Fig. 5). The daytime LST pattern shows changes between the 2000–2009 and 2010–2019 time periods that are proportional to urban and built-up land cover change that occurred during the corresponding periods (Fig. 5a). A local maximum of spatial average LST occurs over the urban core and to the northeast of the city meteorological station location (open circle), both during the 2000–2009 (Fig. 5a) and 2010–2019 (Fig. 5b) time periods. The local maximum of decadal average daytime LST increased from \sim 306 K during the 2000–2009 period to >308 K during 2010–2019. Regions of enhanced daytime LST, as defined by pixel locations surrounding the local maximum and with decadal average LST values of 305 K or greater, show substantial growth between the 2000–2009 and 2010–2019 time periods, increasing from 13 to 58 km². The local maximum of nighttime LST within the urban core coincides with locations of corresponding daytime LST maximum for both the decadal periods (Fig. 5c, d). Areal extent of regions of enhanced urban nighttime LST (defined by contiguous pixel locations surrounding the local maximum with mean decadal LST > 297 K) also grow between the 2000–2009 and 2010–2019 time periods, increasing from 30 to 77 km². An increase in daytime LST is also evident along the coast, especially along the central coastal region, where the second meteorological station utilized in this study is

Table 2

LULC change matrix for the Thiruvananthapuram municipal corporation showing land cover transitions between the years 2001 and 2019 derived using the MODIS land cover type dataset. See section 2.1 for the expansion of acronyms used in the table headers that indicate International Geosphere-Biosphere Programme land cover classifications. The horizontal shaded row in the table shows the areal coverage of IGBP land cover classes in km² for the year 2001, while the vertical shaded column shows the same, except for the year 2019. Cells in each column show the area of a given land cover type in 2001 (shown by column header) converted to other land cover types (shown by row header) in 2019. Shaded diagonal elements are the area of each land cover type that remains unchanged between the years 2001 and 2019.

	2001	EB	WS	SV	GL	WL	CL	UB	CN	WB
2019		4.50	28.06	10.06	4.38	5.56	1.63	46.00	119.00	1.56
EB	0.00	0.00	0.00	0.00	0.00	0.00	0.00	0.00	0.00	0.00
WS	18.38	3.69	10.56	0.88	0.63	2.50	0.00	0.00	0.13	0.00
SV	9.13	0.00	3.06	3.06	0.63	0.75	0.00	0.00	1.63	0.00
GL	1.31	0.19	0.25	0.13	0.06	0.69	0.00	0.00	0.00	0.00
WL	1.25	0.00	0.13	0.00	0.00	1.13	0.00	0.00	0.00	0.00
CL	0.75	0.00	0.00	0.00	0.00	0.00	0.00	0.00	0.75	0.00
UB	73.88	0.00	2.56	4.38	0.81	0.00	1.63	46.00	18.50	0.00
CN	114.50	0.63	11.50	1.63	2.25	0.50	0.00	0.00	98.00	0.00
WB	1.56	0.00	0.00	0.00	0.00	0.00	0.00	0.00	0.00	1.56

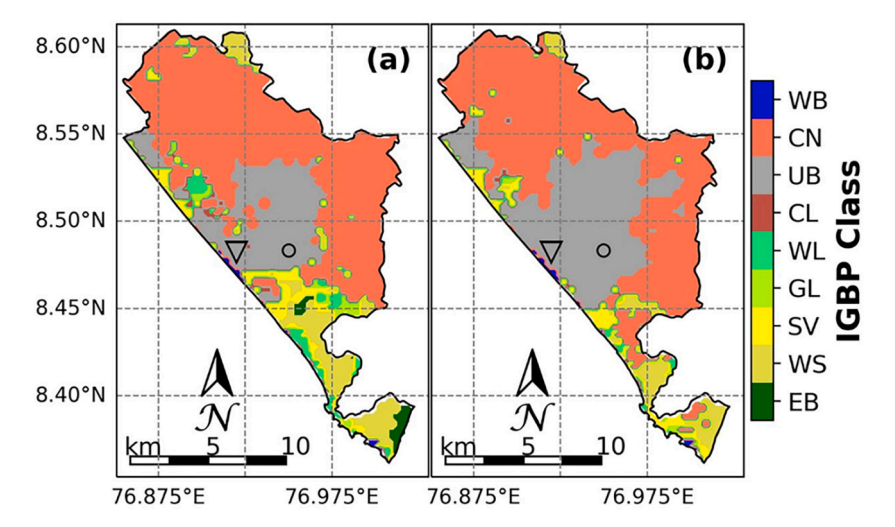


Fig. 3. Panels (a) and (b) show MODIS derived IGBP classification for years 2001 and 2019 respectively. The triangle and circular markers indicate the locations of the coastal and inland meteorological stations, respectively.

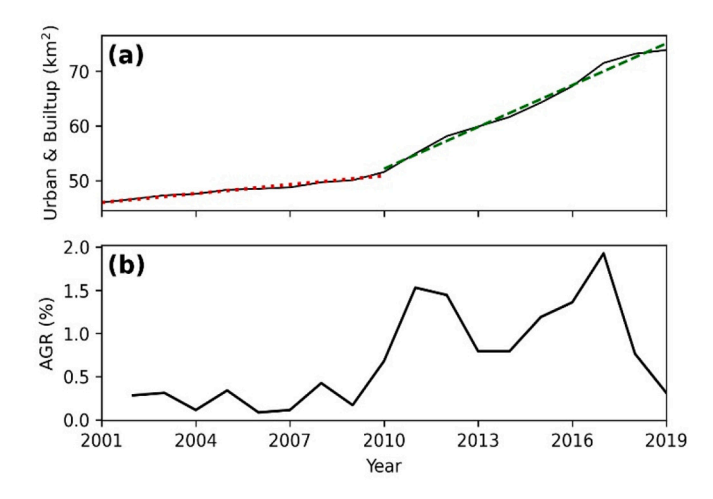


Fig. 4. Area of urban and built-up land cover within TMC as a function of the year is shown in panel (a). The red dotted and green dashed lines are linear fit to urban and built up land cover growth during the time period 2001–2010 and 2010–2019. Annual growth rate (AGR) as a function of the year is shown in panel (b). (For interpretation of the references to colour in this figure legend, the reader is referred to the web version of this article.)

located (triangle in Fig. 5a, b). Decadal average NDVI show patterns of vegetation loss (Fig. 5e, f) that correlate well with patterns of urban growth (Fig. 3a, b) and LST changes (Fig. 5a, b, c, d) between 2000 and 2009 and 2010–2019 decadal periods.

We also examined how daytime, nighttime LST, and NDVI changed for locations that transitioned to urban and builtup land cover class during the second decade of this century (2010–2019). For such locations, we found that the mean of decadal average daytime and nighttime LST increased from 303.90 to 304.83 K (change of 0.93) and from 296.73 to 297.34 K, respectively. Similarly, the mean of the decadal average NDVI for these locations decreased from 0.62 to 0.55 (change of -0.07).

We also examined the time trends of LST. Mann-Kendall test, applied to monthly and area-averaged time series of day and nighttime LST (Fig. 6) with seasonality removed, shows statistically significant (p < 0.01) and increasing monotonic trends. Over the two decades, nighttime LST increased at a slightly higher rate than daytime LST, as indicated by computed Sen slope of 0.00335 and 0.00367 °C month⁻¹ for day and nighttime LST respectively.

Since land cover and vegetation change analysis (Figs. 3, 5) suggest a potential link to LST trends, we examined processes through which these changes impact LST. LULC change can impact LST through modification of a variety of factors tied to the surface energy budget, including changes in albedo, emissivity, roughness length, and moisture availability (Ramamurthy and Bou-Zeid, 2017; Rath et al., 2022). To examine the alteration of albedo and emissivity due to urbanization, we compared the decadal average spatial patterns of MODIS-derived broadband albedo and emissivity for the 2000–2009 and 2010–2019 time periods (Fig. 7). These spatial maps show urban growth leading to an increase in albedo and a decrease in emissivity, with the ceiling of changes in decadal average values of

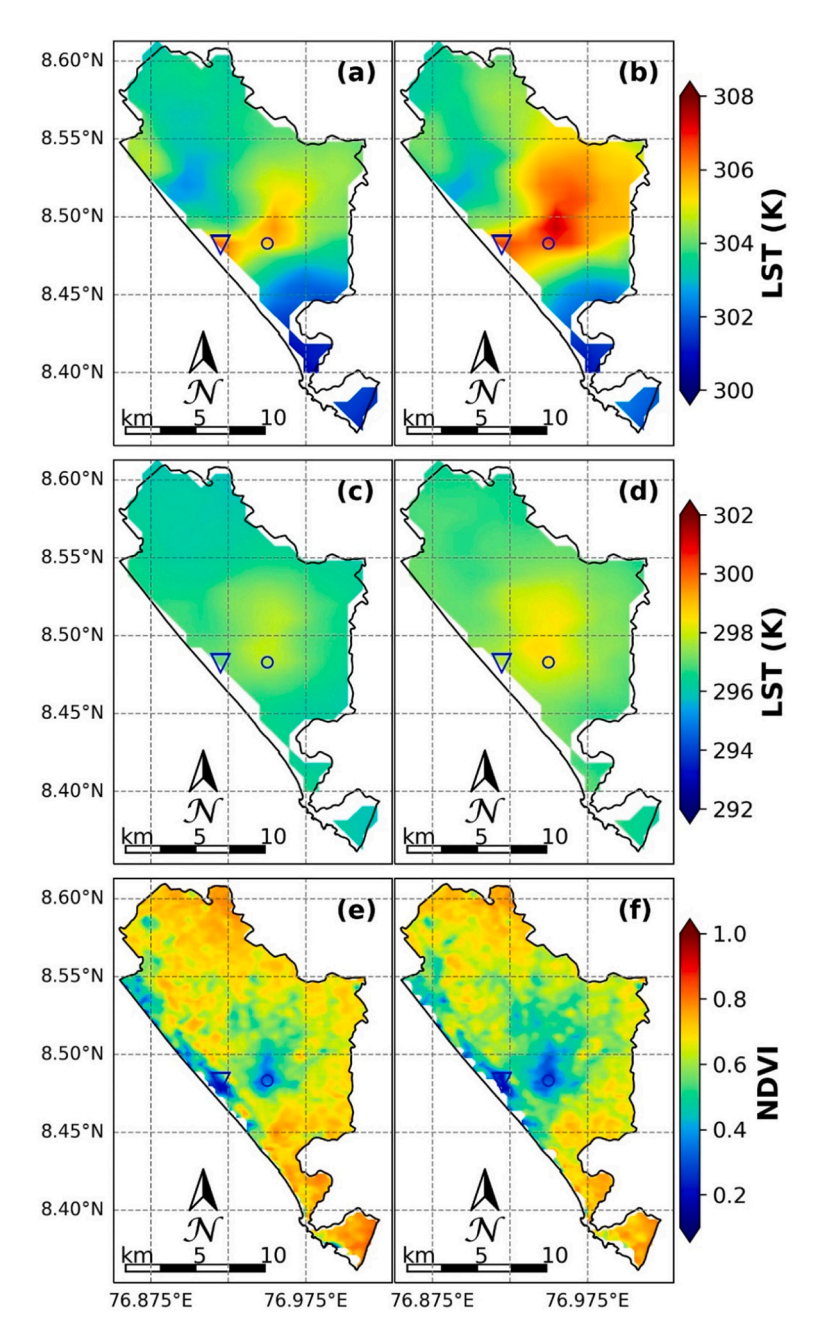


Fig. 5. Ten year average spatial distribution of MODIS derived daytime LST, nighttime LST, and NDVI for TMC are shown in the panels (a,b), (c,d), and (e,f), respectively. The triangle and circular markers indicate the locations of the coastal and inland meteorological stations, respectively.

albedo and emissivity being \sim 0.025 (from 0.125 to 0.15) and - 0.005 (from \sim 0.98 to 0.975), respectively. Assuming maximum decadal average LST value of 308 K (Fig. 5b) and using Stefan-Boltzmann's law for a gray body, it can be inferred that a decrease in emissivity from 0.98 to 0.975 alone can account for a maximum temperature increase of \sim 0.4 K. An increase in albedo will result in a decrease in net energy input at the surface and consequently, a cooling effect on LST. Therefore, the maximum increase in LST resulting from the combined impact of albedo and emissivity change has to be <0.4 K. However, the decadal average patterns (Fig. 5a, b) show LST changes over 3 K at locations of urban growth. This suggests that changes in surface roughness or moisture availability associated with urban growth are the major factors causing increases in LST.

Prior studies show that urbanization and the associated increases in roughness are often accompanied by decreasing trends of near-surface wind speeds (Liu et al., 2018; Ongoma et al., 2013; Rajeswari et al., 2021). Therefore, we examined the time series of monthly average wind speeds from the inland meteorological station for the presence of a decreasing trend (Fig. 8). Seasonal Mann-Kendall test applied to the monthly average time series of wind speed detected a statistically significant, monotonic decreasing trend of wind speeds

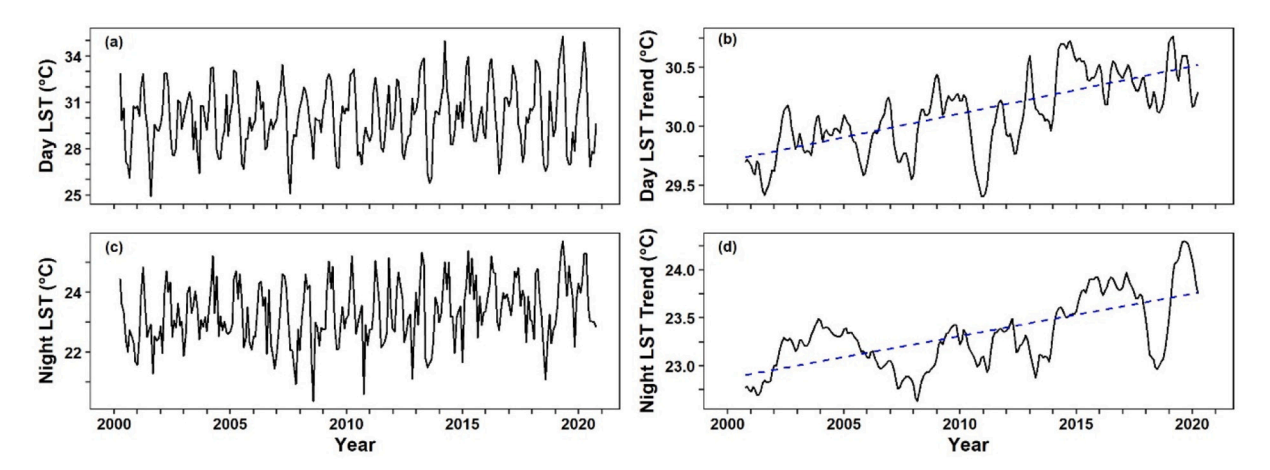


Fig. 6. Time series of monthly area averaged daytime and nighttime LST for TMC are shown in panels a and c respectively. Corresponding trend of the variables obtained after removing seasonality is shown in panels b and d respectively. Dashed blue line in panels b and d shows linear trend, based on Sen slope and intercept. (For interpretation of the references to colour in this figure legend, the reader is referred to the web version of this article.)

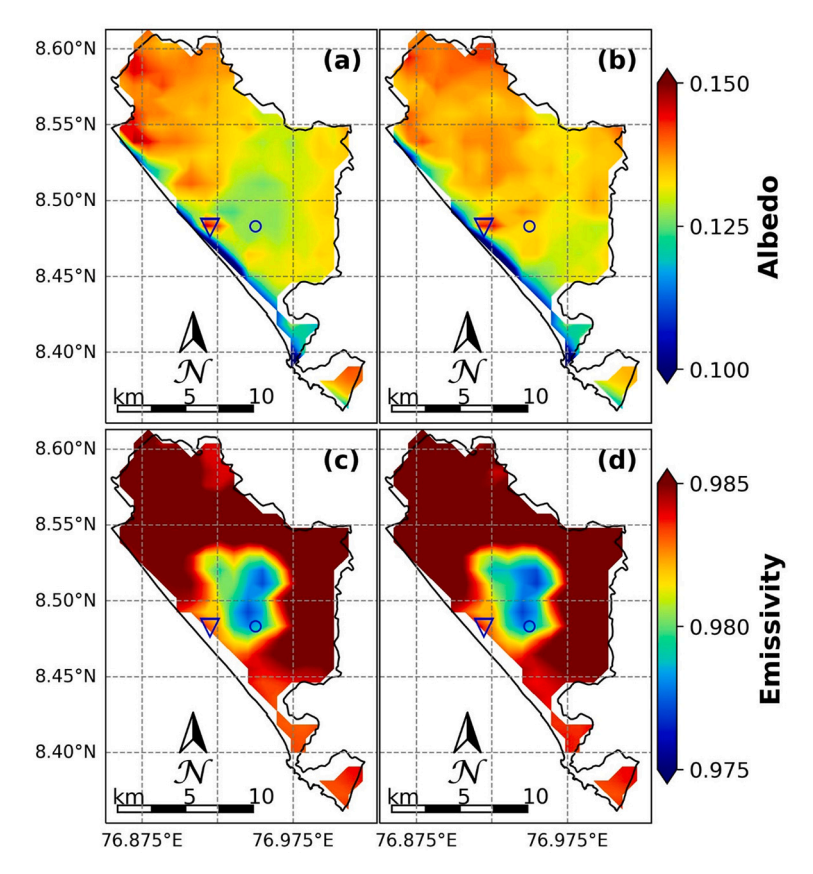


Fig. 7. Ten year average spatial distribution of MODIS derived broadband albedo and emissivity are shown in the first (a,b) and second (c,d) row. The left and right panel on each row is for the decadal time periods of 2000–2009 and 2010–2019, respectively. The triangle and circular markers indicate the locations of the coastal and inland meteorological stations, respectively.

 $(\tau = -0.471, p \text{ value} < 0.0001)$, with the Sen slope for the seasonally decomposed trend of $-0.0236 \text{ ms}^{-1} \text{ year}^{-1}$. We also applied the seasonal Mann-Kendall test to the time series of two-meter wind speeds from the MERRA-2 grid point over TMC (G_2), which also detected a statistically significant decreasing trend for the period of 1980–2022 ($\tau = -0.065, p \text{ value} = 0.03$). The Sen slope for the seasonally decomposed trend of $-0.0032 \text{ ms}^{-1} \text{ year}^{-1}$, which is one order of magnitude smaller than the same metric computed for the

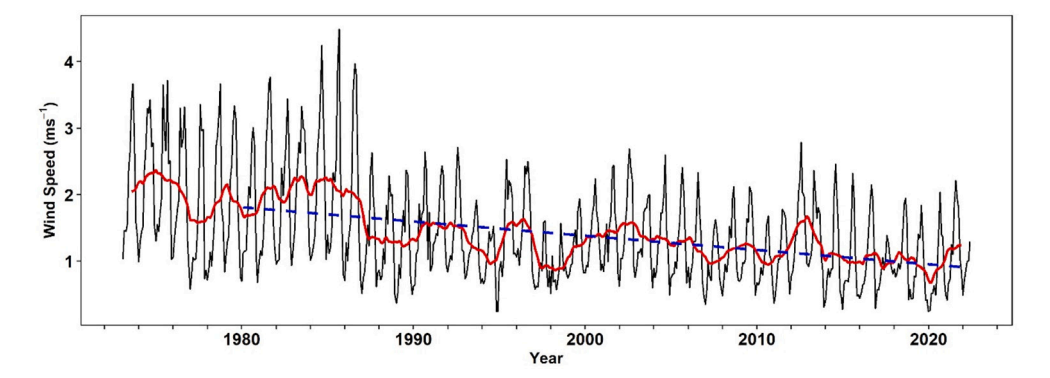


Fig. 8. Monthly average time series of wind speed for the Thiruvananthapuram inland station for the time period of March 1973 to May of 2022 is shown using the black curve. Red curve is the trend component of seasonal decomposition of the time series. Blue dashed line is the linear trend based on the Sen slope computed for the trend component (red curve) of seasonal decomposition of the time series. (For interpretation of the references to colour in this figure legend, the reader is referred to the web version of this article.)

same period for wind speed time series for the inland station ($-0.0214 \, \mathrm{ms}^{-1}$). This comparison shows that the strong decreasing trend of wind speed observed at the inland station is not driven by changes in large-scale dynamical forcing, but by local increases in surface roughness associated with urbanization.

One of the implications of the above-described analysis is that increase in surface roughness leads to enhancement in the turbulent transport of heat from the surface, which tends to reduce LST. Therefore, the magnitudes of observed LST changes over TMC cannot be explained by the combined impact of albedo, emissivity and surface roughness alterations caused by urbanization. Consequently, the dominant cause for increased LST has to be a change in surface moisture availability caused by urbanization.

A decrease in moisture availability as the dominant cause is supported by analysis showing substantial decreases in NDVI, with the spatial patterns of NDVI change (Fig. 5e, f) well correlated with the patterns of urban growth (Fig. 3a, b). Reduction of deep-rooted vegetation and replacement by impervious surface leads to a higher proportion of the net energy input being utilized for heating

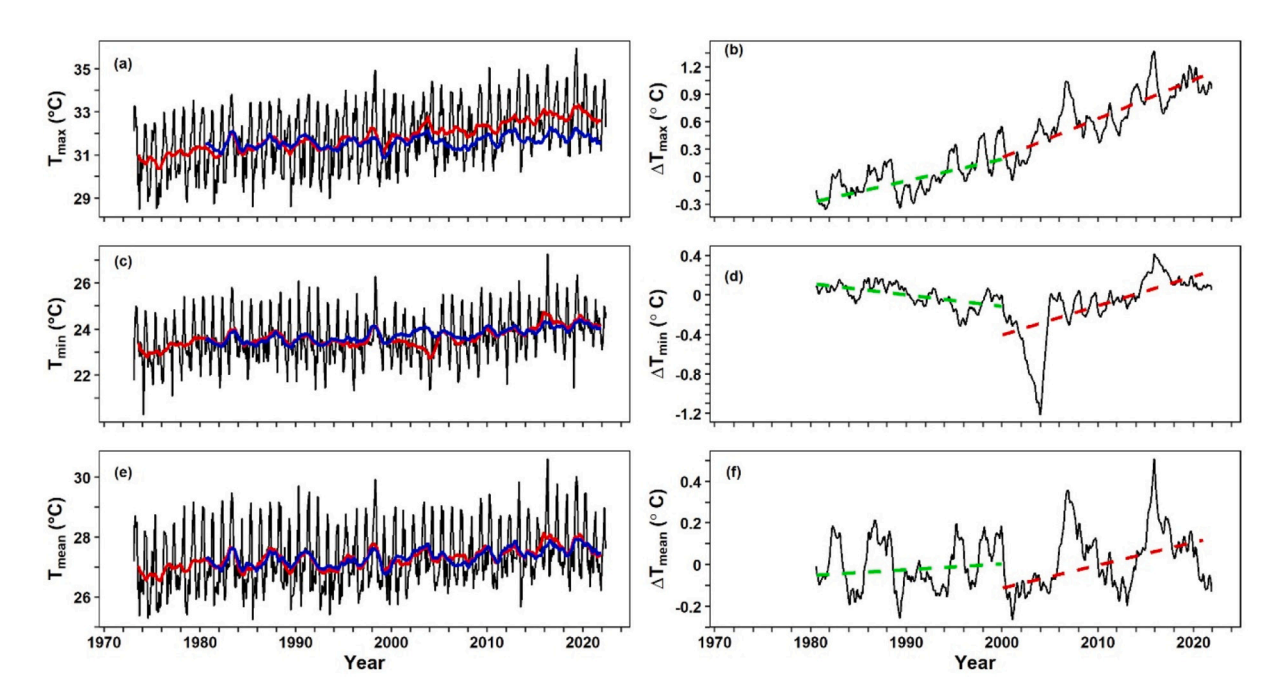


Fig. 9. Monthly average time series (1973–2022) of observed maximum, minimum, and average temperatures for the Thiruvananthapuram inland station are shown using black lines in panels a, c and e. Red lines in the panels a, c and e are the trend components of seasonal decomposition of the time series shown in black. Blue lines in panels a, c and e are the trend components of seasonal decomposition of the GLM_{Tmx} , GLM_{Tmn} and GLM_{Tav} predicted time series. The black lines in panels b,d and f are trend components of seasonal decomposition of residuals (difference between observed and GLM predicted time series) for maximum, minimum average temperature. Blue and red dashed lines in panels b, d, and f are the linear trend lines based on the Sen slope computed for 1980–1999 and 2000–2022 time periods. (For interpretation of the references to colour in this figure legend, the reader is referred to the web version of this article.)

the surface rather than evaporation and transpiration, causing higher LST.

5.2. Statistical modeling analysis of surface temperature trends

To examine how changes in surface energy budget affect the atmosphere, we examined long-term time series of monthly averaged maximum, minimum, and mean temperatures (Fig. 9) at 2 m for the inland station, which is located within the urban core (Fig. 3). Seasonal Mann-Kendall tests show statistically significant, monotonic trends for maximum ($\tau = 0.54$, p-value <0.0001), minimum ($\tau = 0.337$, p value <0.0001), and average temperatures ($\tau = 0.303$, p value <0.0001). However, these trends include both large-scale climatic trends and local forcing impacts, including urbanization. Therefore, as discussed in the methodology section, we fit three GLM models, namely GLM_{Tmx}, GLM_{Tmn}, and GLM_{Tav} for predicting monthly mean maximum, minimum, and average temperature for the period of 1980 through 1999 at the inland station location.

 GLM_{Tmx} , GLM_{Tmn} and GLM_{Tav} models, which use MERRA-2 variables to account for large-scale local forcings except for the land cover, are then utilized to predict from 2000 to 2022, which is contrasted by rapid urban growth in the region. Rather than showing the raw predicted time series from these models, for clarity, we show the trend component from the seasonal decomposition of the predicted time series in Fig. 9a, c, and e. These model predictions can be compared against the seasonally decomposed trend for the observed time series (Fig. 9a, c, and e). It can be readily seen that differences between the GLM predictions and observed series are higher during the period 2000–2022. This can be attributed to land cover change, the most dominant local forcing that is not considered in the models.

To quantify the changes that could be attributed to urbanization, we computed the difference (residual) between the observed and predicted time series. Next, we subjected the 1980–1999 and 2000–2022 periods of this residual time series to the seasonal Mann-Kendall test for detecting monotonic trends; the results of which are shown in Table 3. We also seasonally decomposed the residual time series for maximum, minimum and average temperature, and the corresponding trend components are shown in Fig. 9b, d, and f, respectively. Sen slopes for these trend components are computed separately for the periods 1980–1999 and 2000–2022, with the values being given in Table 3 and linear trend lines shown in Fig. 9b, d, and f.

The residuals for maximum temperature (Fig. 9b) show statistically significant and increasing monotonic trends both before and after the year 2000 (Table 3). However, the Sen slope value is ∼1.8 times larger for the 2000–2022 time period, when TMC experienced drastic growth in urban and built-up land cover. Our analysis shows that the upper limit of urbanization impact on maximum temperature is ~1 °C increase over the period of 2000–2022. A statistically significant decreasing trend is found for minimum temperature (Fig. 9d, Table 3) during 1980-1999 followed by a statistically significant increasing trend afterward. The magnitude of the Sen slope for the 2000–2022 period is an order of magnitude greater compared to that for the 1980–1999 time period and urbanization can account for ~0.4 °C increase in minimum temperature in the urban core region of TMC. Another notable feature found in the time series of minimum temperature residuals (Fig. 9d) is the strong negative anomaly during the 2002-2003 time period. The forcing factors responsible for this feature are unknown, but it could be due to a variety of factors. Nocturnal temperatures are sensitive to subtle changes in longwave radiative forcing, which can be affected by atmospheric water vapor, aerosols and clouds, especially upperlevel cirrus. Additionally, 2002-2003 was subject to a moderate El Nino. Our analysis also shows a small increasing trend for the average temperature residuals (Fig. 9d, Table 3) for the 1980–1999 time period, followed by a statistically significant increasing trend that can account for ~0.22 °C increase over 20 years. Statistical modeling, therefore, shows that while an increasing trend attributed to urbanization is found for maximum, minimum and average temperatures, the dominant impact is an increase in maximum temperature. Model predictions show that urbanization exacerbates increasing trends of maximum, minimum and average temperature, caused by large-scale climate forcing.

5.3. Impact of urbanization on daytime patterns of surface meteorology

We also compared decadal average daytime patterns of surface wind speed, wind direction, temperature, water vapor mixing ratio, and relative humidity for coastal and inland stations during the 2000–2009 and 2010–2019 time periods (Fig. 10). Note that the inland station is located within the urban core, while the coastal station is located along the periphery (Fig. 3). While the urban and built-up land cover fetch in the vicinity of both the stations substantially increase by 2019, changes are disproportionately higher for the coastal station.

Table 3Monotonic trend analysis for differences between observed and GLM predictions for maximum, minimum and average air temperatures for the Thiruvananthapuram inland stations.

Time Series	Test/Metric	Time Period	Time Period	
		1980–1999	2000–2022	
T _{max} , residual	Seasonal Mann-Kendall	$\tau=0.168, p\text{-value} < 0.001$	$\tau = 0.303$, p-value < 0.0001	
T _{max} , residua1, seasonal decomposition trend	Sen slope	$0.0237~^{\circ}\text{C Y}^{-1}$	$0.0423~^{\circ} \mathrm{C}~\mathrm{Y}^{-1}$	
T _{mn} , residual	Seasonal Mann-Kendall	$\tau = -0.156$, p-value < 0.001	$\tau = 0.327$, p-value < 0.0001	
T _{mn} , residual, seasonal decomposition trend	Sen slope	$-0.0028~^{\circ}\text{C Y}^{-1}$	0.0296 °C Y ^{−1}	
T _{av} , residual	Seasonal Mann-Kendall	$\tau = 0.0147$, p-value < 0.8	$\tau = 0.123$, p-value < 0.001	
Tav, residual, seasonal decomposition trend	Sen slope	0.0028 °C Y ⁻¹	$0.011~^{\circ} C~Y^{-1}$	

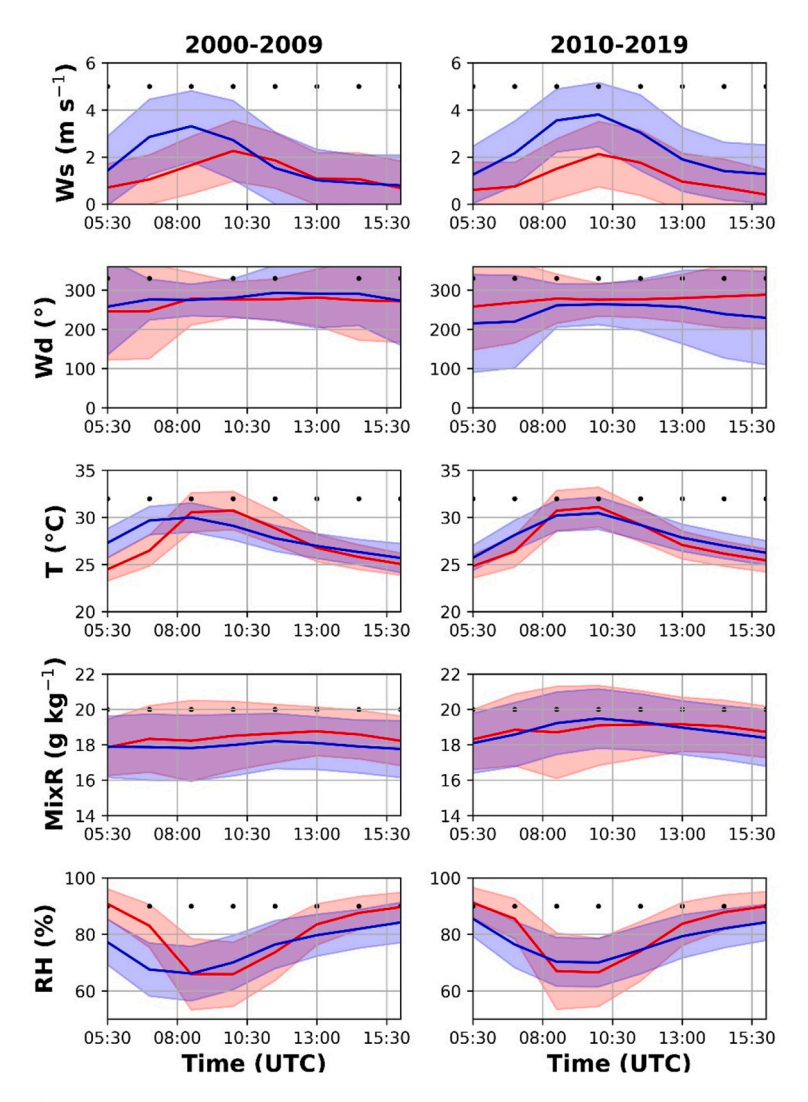


Fig. 10. Mean diurnal curves for 2000–2009. Blue curves are the coastal station, and red curves are the city station. Black dots indicate times during which differences between the sites are statistically significant (p < 0.05). Shading is a one standard deviation envelope. Times are Local Time (UTC + 5.5 h). (For interpretation of the references to colour in this figure legend, the reader is referred to the web version of this article.)

We found potential effects of this land cover change reflected in the decadal average daytime cycles (Fig. 10), with the most drastic impacts being observed at the coastal station. Between the first (2000–2009) and second decadal period (2010–2019) of analysis, the daytime patterns over the coastal station experienced a phase shift, with maximum wind speed and temperature and minimum of relative humidity occurring later in the day during the second decade. Wind direction, before ~8:30 AM and after ~2:30 PM, is also found to have changed at the coastal station during the second decadal period. With this phase shift happening during the second decade, when TMC experienced drastic urbanization, average daytime cycles of wind, temperature, and relative humidity at the coastal station became more in phase with the corresponding cycles observed at the inland station. This is evidenced by the increase in correlation between average cycles for variables at both stations from the 2000–2009 to 2010–2019 decadal periods. For example, the correlation between average temperature cycles at both stations increases from 0.66 to 0.91 and that for wind speed increases from 0.43 to 0.53 from 2000 to 2009 to 2010–2019.

Additionally, the mean maximum temperature at both stations increased between the first and second decadal periods, changing from 30.7 to 31.1 °C and 30.0 to 30.5 °C at the inland and coastal stations, respectively (Fig. 10). However, the mean maximum daytime wind speed shows an increase from 3.3 m/s to 3.8 m/s at the coastal station, as opposed to decreasing from 2.3 m/s to 2.1 m/s at the inland station. At both sites, the occurrence of daytime maximum temperature and wind speeds roughly coincide with the wind direction being westerly. This is indicative of the intensification of local sea-breeze circulation, and the baroclinicity driving it being maximized when the land-sea temperature contrast is at its peak. Thus, the increase in maximum decadal average daytime wind speed at the coastal station is indicative of the strengthening of the sea-breeze circulation. On the other hand, the inland station wind speed decrease suggests increased roughness, convergence and modified inland propagation of the sea breeze.

During the 2000–2009 period, the water vapor mixing ratio at the inland station is consistently higher compared to the coastal station. But during 2010–2019, the water vapor mixing ratio at both the stations increased and shows less difference, except between 8 and 10:30 UTC (13:30–16 LT) when the inland station has smaller values. The overall enhancement of the water vapor mixing ratio (in the range of 0.5-1 g $\rm kg^{-1}$) at both stations during the second decade could be readily explained by increased water vapor carrying capacity, due to higher temperatures. The second decade's 8–10:30 UTC (13:30–16 LT) depression in water vapor mixing ratios at the inland station could be potentially caused by a reduction in vegetation cover caused by urbanization. Another factor that could be responsible for this depression is the alteration in the inland propagation of the sea breeze. These changes in atmospheric water vapor led to a second-decade increase of 5% relative humidity at the coastal station during the hours of the occurrence of maximum temperature. However, due to smaller changes in the water vapor mixing ratio, relative humidity at the inland station during the hours of the occurrence of maximum temperature do not fluctuate much between the first and second decade.

6. Discussion

Our analysis found that TMC, a Tier-2 coastal city in India, experienced a drastic increase in urban and built-up land cover during the last two decades. We found the growth in the area of urban land cover has a statistically significant impact on urban climate, caused primarily by a reduction in vegetation cover and thus surface moisture availability. As deep-rooted vegetation is replaced by impervious surfaces, less of the net-radiative energy received at the surface is utilized for evapotranspiration, leading to an increase in sensible heat flux and Bowen ratio. One of the urban climate impacts of relevance caused by this change is the enhancement of large-scale climate trends of increasing air temperature, especially the daily maximum temperature. We estimate that the urban growth of TMC over the last two decades has added ~1 °C to the large-scale warming trend affecting the region, with the thermal comfort being further degraded due to increased relative humidity. This is consistent with the Intergovernmental Panel on Climate Change (IPCC) Sixth Assessment Report (AR6) finding that anthropogenic influences potentially contribute to doubling the likelihood of heat wave occurrences in Asia (IPCC, 2022). Note that a recent study found that a 0.5 °C increase in mean temperature can increase the probability of heat-related mortality events involving 100 or more people in India by 146% (Mazdiyasni and Coauthors, 2017). In this context, urbanization adding a 0.22 °C increase in mean temperature has serious public health implications.

Another urban climate impact of importance identified by our study is a modification of the sea breeze circulation. Our analysis suggests that the increase in urbanization is strengthening the sea breeze circulation over TMC, but with inland propagation affected by enhanced convergence closer to the coast. This could result in increased rainfall in these areas, which when coupled with a larger areal extent of impervious surface, increases the potential for urban flooding. Strengthening of the sea-breeze circulation is consistent with prior studies that show the intensity of sea-breeze is sensitive to time-integrated sensible heat fluxes along the coast (Kala et al., 2010). Our analysis shows a substantial increase in urban and built-up land cover along the coast and the associated increase in sensible heat flux could be the cause for the strengthening of the sea-breeze circulation. However, further inland, wind speeds decrease due to increased roughness, enhancing convergence, cloud formation and rainfall.

Since our analysis shows that reduction in surface moisture availability (due to a drastic decrease in vegetation cover) is the primary driver of changes in urban climate, the most effective strategy to mitigate these effects is to increase the urban green cover and reduce nonessential impervious surface area (paving of residential areas in specific). Prior studies show that paving of residential gardens/yards can be a major contributor to the growth of impervious surface, with one study showing it accounting for ~75% of the increase in impervious area over a suburban area of Leeds, England from 1971 to 2004 (Perry and Nawaz, 2008). Hydrological modeling examining the impact of this increase in paved residential gardens found a resultant 12% increase in runoff. Anecdotal accounts suggest that the paving of residential yards could be an important contributor to the increase of impervious surface area within Indian SMSCs such as TMC. Studies utilizing very high-resolution satellite observations, coupled with small-scale hydrological modeling are needed to verify if this is indeed the case.

While our data fusion and analytics approach identifies statistically significant trends and provides clear indications of urban growth affecting the sea breeze circulation, further investigation using physically based models are needed to validate and gain a clear understanding of processes through which urbanization affects local climate.

Lastly, our study findings are very relevant to India, where urban expansion is at its peak. It is projected that by 2030 nearly half of the 100 million new urban dwellers of India will reside in medium-sized cities (Birkmann et al., 2016; Shaban et al., 2020), including many along coastal regions. Since the growth of SMSCs is often fast-paced (as demonstrated here for TMC) planning for growth is difficult, including following the United Nations' sustainable development goal to "make cities and human settlements inclusive, safe, resilient, and sustainable". In this context, Urban Integrated Services (UIS) can be a beneficial tool in planning for the growth of SMSC (Baklanov and Coauthors, 2020). The data fusion and analytics approach used in this study can potentially serve as an important component in such a framework for accounting climatic impacts of urban growth. Note that all of these datasets are available on the cloud and can be accessed using cloud computing platforms and technologies. Our data fusion approach was implemented on Google Colab and utilized datasets available through Google Earth Engine and NASA and NOAA datasets hosted on the cloud. This approach frees the user from maintenance of data, computing hardware, and software making the framework accessible to all levels of decision-makers.

7. Conclusions

Prior studies on the environmental impacts of urbanization in India mostly focused on megacities. However, there are several SMSCs, especially along the coastal regions, that are expected to grow at a fast pace, rendering planning for growth difficult. Further

complicating planning efforts is the lack of understanding of the environmental impacts of urban growth, which is expected to be exacerbated in coastal settings. We utilized fusion and analytics of NASA MODIS satellite-derived land products, NASA MERRA-2, and NOAA *in-situ* meteorological data to quantify the multi-decadal growth of urban and built-up land cover over TMC (Tier-2 coastal city in India), associated changes in land-atmosphere interactions, and how it affects urban climate. The major conclusions from this study are as follows:

- 1. TMC experienced fast-paced growth, especially during the last decade, with the urban and built-up land cover area increasing by ~48% between 2010 and 2019. Note that the pace of growth of TMC, belonging to the SMSC category, is larger than those experienced by some of the megacities during a similar period. For example, consider the pace of urbanization of Delhi, Mumbai and Kolkata, three megacities in India. Urban and built-up land cover in Delhi, Mumbai and Kolkata increased only by 23.9% (Salem et al., 2021), 16.6% (Shahfahad et al., 2021) and 16.5% during 2010–2020, 2000–2015 and 2007–2017, respectively.
- 2. Urban growth over TMC during the last two decades resulted in increased albedo, decreased emissivity, and an increase in surface roughness. Both daytime and nighttime LST show statistically significant increasing trends during this period. Order-of-magnitude reasoning shows that the dominant cause for the increasing LST trends is a decrease in surface moisture availability (and an increase in Bowen ratio), a finding supported by a satellite-detected decrease in vegetation cover.
- 3. Our analysis shows that urban growth accounts for \sim 1 °C, \sim 0.4 °C, and \sim 0.22 °C increases in monthly average maximum, minimum, and average temperature over the last two decades and adds to the positive large-scale climate trends of these variables. Note that our results showing smaller increases in minimum compared to maximum temperature is inconsistent with prior studies (e.g., Karl et al., 1988). While nocturnal minimum temperature is sensitive to a variety of factors and thus trends can differ regionally and temporally, limitations of statistical methodologies cannot be ruled out.
- 4. Near the coast, relative humidity and water vapor mixing ratio were both found to increase in response to urban growth and large-scale trends of increasing temperature and thus, deterioration of thermal comfort. However, within the urban core, a decrease in vegetation cover and evapotranspiration causes a reduction in the water vapor mixing ratio during the afternoon hours, which potentially mitigates relative humidity increase compared to the coastal location.
- 5. Urban growth along the coast leads to a shift of daytime cycles of meteorological variables to be more in phase with the same at the urban core. An increase in daytime maximum wind speed at the coastal location and a decrease at the urban core suggests a strengthening of sea-breeze circulation and altered inland propagation with increased convergence closer to the coast.

Our data fusion and analytic approach, implemented using cloud computing methodologies, could be readily utilized in frameworks such as Urban Integrated Services (UIS) to plan for sustainable growth of SMSCs and can be adapted for a variety of applications (Grimmond and Coauthors, 2020).

Our findings, especially urban impacts on the sea breeze and potentially rainfall distribution, need to be further investigated and validated using numerical modeling. However, one of the challenges related to numerical models is their difficulty in replicating the location of isolated convection. A dense network of observations (Hu et al., 2016; Muller et al., 2013) that straddle periods before and after urban growth is required to mitigate this issue. Modeling urban growth and strategically establishing dense observational networks in areas in which urban growth will occur in the future, is needed for this purpose.

CRediT authorship contribution statement

Udaysankar S. Nair: Conceptualization, Methodology, Investigation, Software, Writing – original draft, Supervision, Funding acquisition. **Christopher Phillips:** Methodology, Investigation, Software, Writing – review & editing. **Sukanya Dasgupta:** Methodology, Investigation, Writing – review & editing. **Chandana Mitra:** Conceptualization, Supervision, Writing – review & editing, Funding acquisition.

Declaration of Competing Interest

The authors declare that they have no known competing financial interests or personal relationships that could have appeared to influence the work reported in this paper.

Data availability

All datasets are publicly available

Acknowledgements

Udaysankar Nair acknowledges support from the NSF CAREER Grant AGS-1352046, Google Earth Engine Faculty Award, NASA Grant 80MSFC22M0004 and NASA Grant NNH19ZDA001N-IDS

References

Anurose, T.J., Subrahamanyam, D.B., Sunilkumar, S.V., 2018. Two years observations on the diurnal evolution of coastal atmospheric boundary layer features over Thiruvananthapuram (8.5° N, 76.9° E), India. Theor. Appl. Climatol. 131, 77–90. https://doi.org/10.1007/s00704-016-1955-y.

- Baklanov, A., Coauthors, 2020. Integrated urban services: experience from four cities on different continents. Urban Clim. 32, 100610 https://doi.org/10.1016/j. uclim.2020.100610.
- Birkmann, J., Welle, T., Solecki, W., Lwasa, S., Garschagen, M., 2016. Boost resilience of small and mid-sized cities. Nature 537, 605–608. https://doi.org/10.1038/537605a.
- Channan, S., Collins, K., Emanuel, W.R., 2014. Global Mosaics of the Standard MODIS Land Cover Type Data, p. 30.
- Dai, A., Trenberth, K.E., Karl, T.R., 1999. Effects of clouds, soil moisture, precipitation, and water vapor on diurnal temperature range. J. Clim. 12, 2451–2473, 10.1175/1520-0442(1999)012<2451:eocsmp>2.0.co;2.
- Didan, K., Munoz, A.B., Solano, R., Huete, A., 2015. MODIS Vegetation Index user's Guide (MOD13 Series). Univ. Arizona Veg. Index Phenol. Lab.
- Gelaro, R., Coauthors, 2017. The modern-era retrospective analysis for research and applications, version 2 (MERRA-2). J. Clim. 30, 5419–5454. https://doi.org/10.1175/JCIJ-D-16-0758.1.
- Grimmond, S., Coauthors, 2020. Integrated urban hydrometeorological, climate and environmental services: concept, methodology and key messages. Urban Clim. 33, 100623 https://doi.org/10.1016/j.uclim.2020.100623.
- Hu, L., Brunsell, N.A., 2013. The impact of temporal aggregation of land surface temperature data for surface urban heat island (SUHI) monitoring. Remote Sens. Environ. 134, 162–174. https://doi.org/10.1016/j.rse.2013.02.022.
- Hu, X.M., Xue, M., Klein, P.M., Illston, B.G., Chen, S., 2016. Full access analysis of urban effects in Oklahoma city using a dense surface observing network. J. Appl. Meteorol. Climatol. 55, 723–741. https://doi.org/10.1175/JAMC-D-15-0206.1.
- Hunt, K.M.R., Menon, A., 2020. The 2018 Kerala floods: a climate change perspective. Clim. Dyn. 54, 2433–2446. https://doi.org/10.1007/s00382-020-05123-7.
- IPCC, 2022. Climate Change 2022: Impacts, Adaptation, and Vulnerability. Contribution of Working Group II to the Sixth Assessment Report of the Intergovernmental Panel on Climate Change. Cambridge University Press. Cambridge University Press, Cambridge, UK and New York, NY, USA, p. 3056. https://doi.org/10.1017/9781009325844.
- Kala, J., Lyons, T.J., Abbs, D.J., Nair, U.S., 2010. Numerical simulations of the impacts of land-cover change on a Southern Sea breeze in south-West Western Australia. Bound.-Layer Meteorol. 135, 485–503. https://doi.org/10.1007/s10546-010-9486-z.
- Karl, T.R., Diaz, H.F., Kukla, G., 1988. Urbanization: its detection and effect in the United States climate record. J. Clim. 1, 1099–1123, 10.1175/1520-0442(1988) 001<1099:UIDAEI>2.0.CO;2.
- Lamb, W.F., Creutzig, F., Callaghan, M.W., Minx, J.C., 2019. Learning about urban climate solutions from case studies. Nat. Clim. Chang. 9, 279–287. https://doi.org/10.1038/s41558-019-0440-x.
- Lawrimore, J.H., Menne, M.J., Gleason, B.E., Williams, C.N., Wuertz, D.B., Vose, R.S., Rennie, J., 2011. An overview of the global historical climatology network monthly mean temperature data set, version 3. J. Geophys. Res. Atmos. 116, 1–18. https://doi.org/10.1029/2011JD016187.
- Liu, J., Gao, Z., Wang, L., Li, Y., Gao, C.Y., 2018. The impact of urbanization on wind speed and surface aerodynamic characteristics in Beijing during 1991\– 2011. Meteorog. Atmos. Phys. 130, 311–324. https://doi.org/10.1007/s00703-017-0519-8.
- Mahmood, R., Coauthors, 2014. Land cover changes and their biogeophysical effects on climate. Int. J. Climatol. 34, 929–953. https://doi.org/10.1002/joc.3736. Mazdiyasni, O., Coauthors, 2017. Increasing probability of mortality during Indian heat waves. Sci. Adv. 3, 1–6. https://doi.org/10.1126/sciadv.1700066.
- Mohan, M., Kandya, A., 2015. Impact of urbanization and land-use/land-cover change on diurnal temperature range: a case study of tropical urban airshed of India using remote sensing data. Sci. Total Environ. 506–507, 453–465. https://doi.org/10.1016/j.scitotenv.2014.11.006.
- Muller, C.L., Chapman, L., Grimmond, C.S.B., Young, D.T., Cai, X., 2013. Sensors and the city: a review of urban meteorological networks. Int. J. Climatol. 33, 1585–1600. https://doi.org/10.1002/joc.3678.
- Nair, U.S., McNider, R., Patadia, F., Christopher, S.A., Fuller, K., 2011. Sensitivity of nocturnal boundary layer temperature to tropospheric aerosol surface radiative forcing under clear-sky conditions. J. Geophys. Res. Atmos. 116, D02205. https://doi.org/10.1029/2010JD014068.
- Nelder, A.J.A., Wedderburn, R.W.M., Journal, S., Statistical, R., Series, S.. Generalized Linear Models Published by: Wiley for the Royal Statistical Society Stable. URL. https://www.istor.org/stable/2344614.
- Ongoma, V., Muthama, N., Gitau, W., 2013. Evaluation of urbanization influences on urban winds of Kenyan cities. Ethiop. J. Environ. Stud. Manag. 6, 223–231. https://doi.org/10.4314/ejesm.v6i3.1.
- Perry, T., Nawaz, R., 2008. An investigation into the extent and impacts of hard surfacing of domestic gardens in an area of Leeds, United Kingdom. Landsc. Urban Plan. 86, 1–13. https://doi.org/10.1016/j.landurbplan.2007.12.004.
- Phillips, C., Nair, U., Christopher, S., 2022. The influence of dust-smoke mixtures on boundary layer processes and nocturnal warming in the Sahel. J. Geophys. Res. Atmos. 127 https://doi.org/10.1029/2021JD036349 e2021JD036349.
- Rajeswari, J.R., Srinivas, C.V., Yesubabu, V., Hari Prasad, D., Venkatraman, B., 2021. Impacts of urbanization, aerodynamic roughness, and land surface processes on the extreme heavy rainfall over Chennai, India. J. Geophys. Res. Atmos. 126 https://doi.org/10.1029/2020JD034017 e2020JD034017.
- Ramamurthy, P., Bou-Zeid, E., 2017. Heatwaves and urban heat islands: a comparative analysis of multiple cities. J. Geophys. Res. 122, 168–178. https://doi.org/10.1002/2016.ID025357
- Rana, P., Krishan, G., 1981. Growth of medium sized towns in India. GeoJournal 5, 33-39. https://doi.org/10.1007/BF00185241.
- Rath, S.S., Panda, J., Sarkar, A., 2022. Distinct urban land cover response to meteorology in WRF simulated pre monsoon thunderstorms over the tropical city of Kolkata. Meteorog. Atmos. Phys. https://doi.org/10.1007/s00703-022-00916-3.
- Rosenzweig, C., Solecki, W., Romero-Lankao, P., Mehrotra, S., Dhakal, S., Ibrahim, S. Ali (Eds.), 2018. Climate Change and Cities: Second Assessment Report of the Urban Climate Change Research Network (ARC3.2)
- Salem, M., Bose, A., Bashir, B., Basak, D., Roy, S., Chowdhury, I.R., Alsalman, A., Tsurusaki, N., 2021. Urban expansion simulation based on various driving factors using a logistic regression model: Delhi as a case study. Sustain. 13, 1–17. https://doi.org/10.3390/su131910805.
- using a logistic regression model: Delhi as a case study. Sustain. 13, 1–17. https://doi.org/10.3390/su131910805.

 Shaban, A., Kourtit, K., Nijkamp, P., 2020. India's urban system: sustainability and imbalanced growth of cities. Sustain. 12 https://doi.org/10.3390/su12072941.
- Shahfahad, M., Rihan, M.W., Naikoo, M.A., Ali, T.M., Usmani, Rahman, A., 2021. Urban Heat Island dynamics in response to land-use/land-cover change in the Coastal City of Mumbai. J. Indian Soc. Remote Sens. 49, 2227–2247. https://doi.org/10.1007/s12524-021-01394-7.
- Smith, A., Lott, N., Vose, R., 2011. The integrated surface database: recent developments and partnerships. Bull. Am. Meteorol. Soc. 92, 704–708. https://doi.org/10.1175/2011BAMS3015.1.
- United Nations, 2018. Department of Economic and Social Affairs, P. D. In: World Urbanization Prospects: The 2018 Revision, Online Edition. https://population.un.org/wup/Publications/Files/WUP2018-Report.pdf.
- Wan, Z., 2014. New refinements and validation of the collection-6 MODIS land-surface temperature/emissivity product. Remote Sens. Environ. 140, 36–45. https://doi.org/10.1016/j.rse.2013.08.027.
- Wan, Z., Zhang, Y., Zhang, Q., Li, Z., 2002. Validation of the land-surface temperature products retrieved from Terra moderate resolution imaging Spectroradiometer data. Remote Sens. Environ. 83, 163–180. https://doi.org/10.1016/S0034-4257(02)00093-7.
- Wang, Z., Zeng, X., Barlage, M., Dickinson, R.E., Gao, F., Schaaf, C.B., 2004. Using MODIS BRDF and albedo data to evaluate global model land surface albedo. J. Hydrometeorol. 5, 3–14. https://doi.org/10.1175/1525-7541(2004)005<0003:UMBAAD>2.0.CO;2.

Wolfe, R.E., Roy, D.P., Vermote, E., 1998. MODIS land data storage, gridding, and compositing methodology: level 2 grid. IEEE Trans. Geosci. Remote Sens. 36, 1324-1338. https://doi.org/10.1109/36.701082.

- Xiao, J., Shen, Y., Ge, J., Tateishi, R., Tang, C., Liang, Y., Huang, Z., 2006. Evaluating urban expansion and land use change in Shijiazhuang, China, by using GIS and remote sensing. Landsc. Urban Plan. 75, 69–80. https://doi.org/10.1016/j.landurbplan.2004.12.005.

 Yang, Q., Huang, X., Tang, Q., 2019. The footprint of urban heat island effect in 302 Chinese cities: temporal trends and associated factors. Sci. Total Environ. 655, 652–662. https://doi.org/10.1016/j.scitotenv.2018.11.171.